



Simultaneously high-rate furfural hydrogenation and oxidation upgrading on nanostructured transition metal phosphides through electrocatalytic conversion at ambient conditions

Xian Zhang^{a,1}, Miaomiao Han^{a,1}, Guoqiang Liu^a, Guozhong Wang^a, Yunxia Zhang^a, Haimin Zhang^{a,*}, Huijun Zhao^{a,b}

^a Key Laboratory of Materials Physics, Centre for Environmental and Energy Nanomaterials, Anhui Key Laboratory of Nanomaterials and Nanotechnology, CAS Center for Excellence in Nanoscience, Institute of Solid State Physics, Chinese Academy of Sciences, Hefei, 230031, China

^b Centre for Clean Environment and Energy, Griffith University, Gold Coast Campus, QLD, 4222, Australia

ARTICLE INFO

Keywords:

VPH
Furfural
Electrocatalytic hydrogenation
Electrocatalytic oxidation
Transition metal phosphides

ABSTRACT

We successfully synthesize Cu₃P nanosheets and granular Ni₂P nanocrystals on the surface of commercial carbon fiber cloth (CFC) (Cu₃P/CFC and Ni₂P/CFC) respectively by a vapor-phase hydrothermal route. The as-synthesized Ni₂P/CFC and Cu₃P/CFC as electrodes all show the bifunctional electrocatalytic performances towards hydrogen evolution reaction (HER) and the oxygen evolution reaction (OER), simultaneously all demonstrating the electrocatalytic activities of the furfural hydrogenation reaction (FHR) and furfural oxidation reaction (FOR) in alkaline media. Comparatively, the Cu₃P/CFC exhibits higher FHR activity with almost ~100% selectivity of the furfuryl alcohol (FAL) product and high Faradaic efficiency (FE) of 92.0%–98.0% over the applied potential range of –0.05 to –0.55 V (vs. RHE), while the Ni₂P/CFC indicates higher FOR activity with almost ~100% selectivity of furoic acid (FA) product and FE of 90.0%–98.0% at the applied potential of 1.2–1.7 V (vs. RHE) in alkaline electrolyte containing 50 mM furfural. The DFT calculations results reveal that the (1–10) dominated Cu₃P can obtain higher hydrogen coverage but restricted H₂ desorption compared to the (001) dominated Ni₂P, therefore the adsorbed active hydrogen (H) atoms from water can be effectively used for the FHR process, resulting in high FE and current density. The superior FOR activity of the Ni₂P/CFC is mainly stemmed from the formed high valence state Ni species during electrocatalysis. Thanks to the superior FHR performance of Cu₃P/CFC and FOR activity of Ni₂P/CFC, a two-electrode H-type electrocatalysis system assembled with the Cu₃P/CFC as cathode and Ni₂P/CFC as anode can be constructed for simultaneously electrocatalytic production of FAL and FA with almost ~100% selectivity in 1.0 M KOH electrolyte containing 50 mM furfural in each chamber under the given experimental conditions, demonstrating high FE of 97%–99%.

1. Introduction

Increasing environmental contamination and excessively consumed fossil fuels have motivated considerable research efforts to developing renewable energy production and storage alternatives [1–3]. In this regard, the conversion of biomass and their derivatives can provide a sustainable pathway to lessen the dependence on fossil fuels-based resources for the production of fuels, chemicals and solvents [4–7]. For example, representative furanic compounds (furfural, and 5-hydroxymethylfurfural), generally produced by acid-catalyzed dehydration of sugars, have great potential as alternative commodity chemicals to petroleum-based platform chemicals [8,9]. However, the chemicals

manufacturing from biomass and their derived platform molecules represent a challenging issue because of limited conversion techniques, poor catalytic performance and product selectivity [3,10,11]. Generally speaking, the conventional hydrogenation or oxidation valorization is accomplished through thermocatalytic conversion processes with high-pressure H₂ or O₂ at high temperature and high pressure conditions employing all kinds of heterogeneous catalysts, usually containing noble metals [8,12–19]. Therefore, the development of new synthetic method with high catalytic activity, high selectivity and lower energy consumption towards biomass platform molecules valorization, is highly desirable and concurrently remains as a huge challenge.

One promising approach is to develop the electrochemical

* Corresponding author.

E-mail address: zhanghm@issp.ac.cn (H. Zhang).

¹ These authors contributed equally in this work.

conversion processes that can convert the biomass platform molecules into high value-added products by employing the sustainable energy (e.g. solar energy etc.) [3,4,20–24], capable of avoiding the explosion of dangerous high temperature and pressure H_2 or the excessive use of high-cost organic molecules hydrogen sources (e.g., isopropanol, triethanolamine and organosilanes) [25,26]. Additionally, the electrochemical conversion approach operating at ambient conditions can utilize the clean and sustainable water as hydrogen source for the hydrogen-transfer hydrogenation and the electrocatalytic oxidation using the active species of electrocatalysts, greatly decrease of the utilization of H_2 source and O_2 /other chemical oxidants [3,21,23,27–29]. However, these processes are strongly dependent on the efficient electrocatalysts with high conversion and Faradaic efficiency (FE), because the electrochemical biomass conversion in aqueous solution always suffers from the competition from water decomposition to produce H_2 and O_2 , thus resulting in low FE and conversion of biomass [4]. In general, an efficient electrocatalytic hydrogenation electrocatalyst must generate the adsorbed active hydrogen (H_{ads}) on the surface of electrocatalyst by the reduction water (Volmer reaction), but necessary for effectively decreasing the H_2 production kinetics of $2H_{ads}$ to H_2 , thus enhancing the electrocatalytic hydrogenation activity [30,31]. In this respect, the competition mechanism between electrochemical hydrogenation of organics and H_2 evolution from water splitting has not been completely ascertained, sometimes controversial. Recently, various metal materials (e.g., Cu, Ag, Pb, Pt, Zn) have been used as the electrodes for the furanic compounds electrocatalytic hydrogenation research [21] (Table S1, Supporting Information), which are primarily focused on the proof-of-concept demonstrations [21,32]. To date, only a few reports have been published on the mechanisms of electrochemical furanic compounds reduction process [3,30,32,33]. For example, Li *et al.* demonstrated that two distinct mechanisms are operable on metallic Cu electrodes in acidic electrolytes, namely, electrocatalytic hydrogenation and direct electroreduction [30]. And Brushett and co-workers reported two electrochemical pathways of the electrocatalytic hydrogenation and hydrodeoxygenation for reduction of oxygenates [32]. Even so, a deep understanding on the electrochemical upgrading reaction mechanism of biomass and their derivatives is still insufficient and deserves a further investigation [31].

Recently, coupling electrochemical water splitting to generate H_2 and organic oxidation reactions in an electrochemical cell has been a promising approach for simultaneous production of clean H_2 fuel and value-added oxidation products, thus maximizing the economic benefits [34–37]. To complete the circuit, the oxidation reactions occurred at the anode require low oxidation overpotential and simultaneous contribute value-added oxidation products. Generally, water oxidation is a typical oxidation half-reaction happened at the anode, but its O_2 evolution reaction kinetics is sluggish and the produced O_2 is not of significant value [20]. For this issue, recently reported studies have integrated the oxidative biomass valorization and H_2 evolution reaction (HER), which not only yields high value oxidation and reduction products at both anode and cathode respectively, but also significantly decreases the voltage input to drive such an integrated electrochemical reaction system [3,37]. Such an integrated system may be extended to concurrently electrochemically synthesize the value-added hydrogenation and oxidation products utilizing the same biomass reactant with high conversion, selectivity and FE. However, the related studies have been rarely reported in literatures.

In this work, taking furfural electrocatalytic conversion as a concept proof model, we report a universal approach of integrating biomass platform molecules oxidation upgrading and simultaneous hydrogenation valorization in an H-type Nafion membrane separated cell. For this, we successfully synthesize the Cu_3P nanosheets and granular Ni_2P nanocrystals on the commercial carbon fiber cloth (CFC) (Cu_3P/CFC and Ni_2P/CFC) respectively by a vapor-phase hydrothermal route. The as-synthesized Ni_2P/CFC and Cu_3P/CFC electrodes not only show the bifunctional OER and HER activities for water splitting, but also both

exhibit furfural hydrogenation and oxidation activities. Comparatively, the Cu_3P/CFC demonstrates higher furfural hydrogenation activity, while the Ni_2P/CFC displays higher furfural oxidation in alkaline media. On the basis of this, the Cu_3P/CFC as the cathode and the Ni_2P/CFC as the anode were assembled into a two-electrode H-type electrochemical cell, exhibiting high furfural conversion to furfuryl alcohol (FAL) on the Cu_3P/CFC and furoic acid (FA) on the Ni_2P/CFC with high selectivity and Faradaic efficiency, comparable or superior to the previously reported electrocatalysts (Table S1, Supporting Information). The corresponding furfural hydrogenation and oxidation mechanisms have been studied and discussed on the basis of the experimental and theoretical calculations results. This work not only demonstrates the feasibility of simultaneous achievement of oxidation and hydrogenation upgrading products from the same organic precursor in a membrane spaced reactor, but also provides a meaningful guidance for designing and fabricating high-efficiency and non-precious metal electrocatalysts for biomass upgrading application.

2. Experimental section

2.1. Material synthesis

2.1.1. Chemicals and materials

Furfural (99%), Furfuryl alcohol (98%) and Furoic acid (98%) were purchased from Aladdin Reagent Company. $NiCl_2 \cdot 6H_2O$, $CuCl_2 \cdot 2H_2O$, potassium hydroxide (KOH), and red phosphorus were purchased from Sinopharm Chemical Reagent Co. Ltd. All the chemicals were used in experiments without further treatment and purification. The commercial carbon fiber cloth (CFC) was provided from Shanghai Hesen Electric Co. LTD.

2.1.2. Fabrication of Cu_3P/CFC and Ni_2P/CFC electrodes

The self-supported copper (or nickel) phosphides on carbon fiber cloth (CFC) were fabricated through a facile vapor-phase hydrothermal (VPH) route, similar with previous work reported by us [34]. A schematic illustration of the fabrication of Cu_3P/CFC and Ni_2P/CFC electrodes was shown in Fig. 1a. Firstly, the CFC ($2.0 \times 1.0 \text{ cm}^2$) was immersed into HNO_3 (65 wt.%) solution for 48 h to increase the surface functional groups (e.g., $-OH$, $-COOH$). After adequately washing with ethyl alcohol and deionized water, the pre-treated CFC was immersed into 6.0 mM Cu^{2+} or Ni^{2+} aqueous solution for 24 h to obtain Cu^{2+} or Ni^{2+} -adsorbed CFC (Cu^{2+} (or Ni^{2+})/CFC). After freeze-drying for 12 h, the Cu^{2+} (or Ni^{2+})/CFC was used as precursor and placed on a Teflon holder (100 mL) containing 0.35 g of red phosphorus and 20 mL of 3.0 M NaOH solution to perform vapor-phase hydrothermal (VPH) reaction. The VPH reaction was operated at 220°C for 0.5 h. After that, the obtained product was denoted as Cu_3P/CFC or Ni_2P/CFC .

2.1.3. Fabrication of Cu/CFC and Pt/CFC electrodes

The Cu/CFC and Pt/CFC electrodes were fabricated through a facile thermal reduction method. In detail, the CFC after nitric acid treatment was immersed into 6.0 mM Cu^{2+} or 6.0 mM chloroplatinic acid ($H_2PtCl_6 \cdot 6H_2O$) aqueous solution for 24 h at normal temperature to obtain Cu^{2+} or chloroplatinic acid-adsorbed CFC. After freeze-drying for 12 h, the Cu^{2+} (or $PtCl_6^{2-}$)/CFC was used as precursor and then heat treating at 350°C for 2 h with a temperature rate of 5°C min^{-1} under 10% H_2 /90% Ar atmosphere. After that, the obtained sample was denoted as Cu/CFC or Pt/CFC .

2.2. Characterizations

The phase structures of the as-prepared electrodes were measured by X-ray diffraction analysis (XRD, Philips X'pert PRO). Field emission scanning electron microscopy (SEM, SU 8020) with an acceleration voltage of 5.0 kV and transmission electron microscopy (TEM, JEOL 2010) equipped with an energy dispersive X-ray spectrometer (EDS

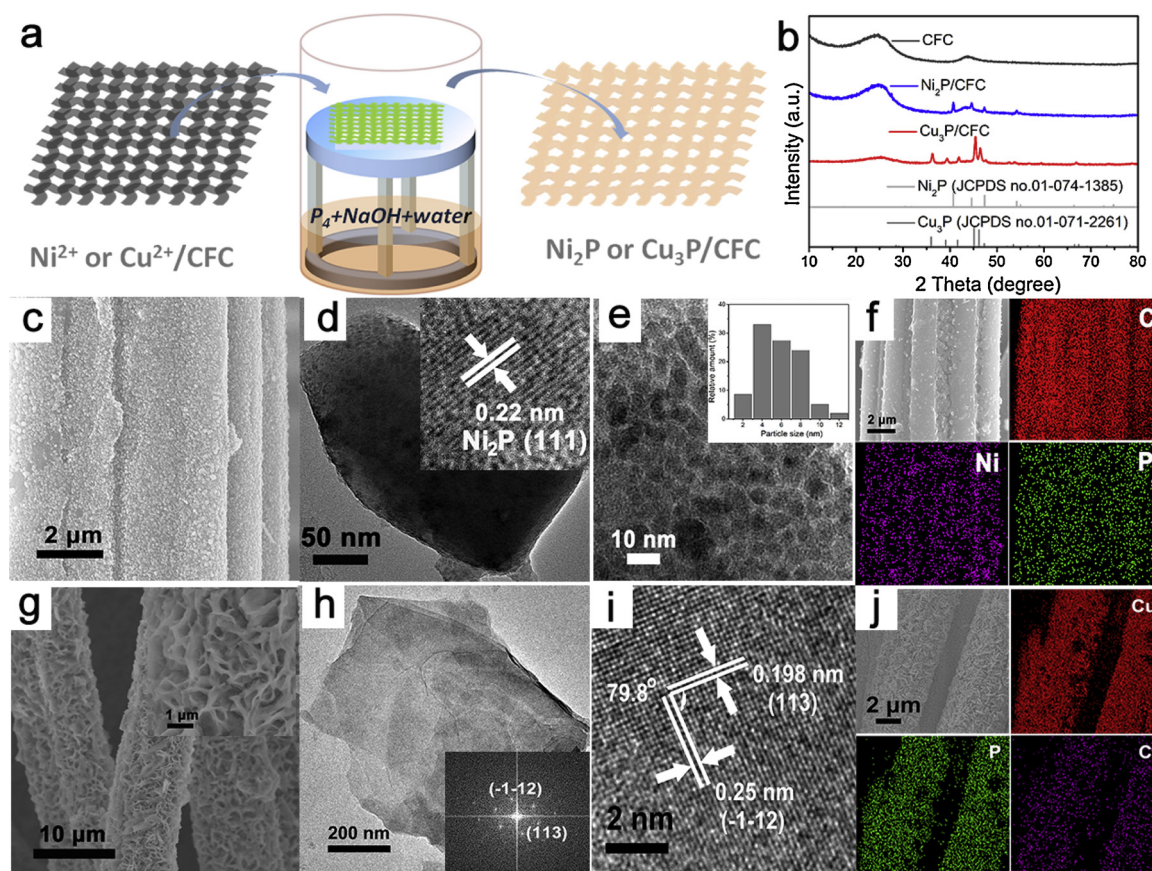


Fig. 1. (a) A schematic illustration of the fabrication process of $\text{Ni}_2\text{P}/\text{CFC}$ and $\text{Cu}_3\text{P}/\text{CFC}$. (b) XRD patterns of CFC, $\text{Ni}_2\text{P}/\text{CFC}$ and $\text{Cu}_3\text{P}/\text{CFC}$. (c) SEM image of $\text{Ni}_2\text{P}/\text{CFC}$. (d–e) TEM images of Ni_2P , the insets in (d) and (e) showing the HRTEM image and the size distribution of Ni_2P nanoparticles, respectively. (f) Scanning electron microscopy-energy dispersive spectroscopy (SEM-EDS) elemental mapping images of $\text{Ni}_2\text{P}/\text{CFC}$. (g) SEM image of $\text{Cu}_3\text{P}/\text{CFC}$. (h–i) TEM and HRTEM images of $\text{Cu}_3\text{P}/\text{CFC}$, the inset in (h) showing the SAED patterns of $\text{Cu}_3\text{P}/\text{CFC}$. (j) SEM-EDS elemental mapping images of $\text{Cu}_3\text{P}/\text{CFC}$.

Oxford, Link ISIS) were used to identify the microcosmic structure and morphology of the as-prepared electrodes. To analyze the elements valence information of as-prepared electrodes, X-ray photoelectron spectroscopy (XPS) analysis was operated on an ESCALAB 250 X-ray photoelectron spectrometer (Thermo, America). $\text{Cu } L_{3,2}$ edge X-ray absorption spectra (XAS) were performed at BL12B-a beamline of NSRL in the total electron yield (TEY) mode.

2.3. Electrochemical measurements

All electrochemical measurements were operated in an H-type electrochemical cell with a Nafion membrane separator. Electrochemical measurements were operated on an electrochemical workstation (CHI 760E). A three-electrode system equipped with gas flow system was used. And the presented current density was normalized to the electrode geometric area. To investigate the catalytic performance of bare CFC, $\text{Ni}_2\text{P}/\text{CFC}$ and $\text{Cu}_3\text{P}/\text{CFC}$ electrodes to electrocatalytically oxidize and reduce furfural, linear sweep voltammetry (LSV) curves were tested with a scan rate of 5.0 mV s^{-1} in 1.0 M KOH solution without and with 50 mM furfural. Chronoamperometry experiments were measured at different applied potentials for the organic substrates electrolysis respectively in a three-electrode system with the as-prepared $\text{Ni}_2\text{P}/\text{CFC}$ or $\text{Cu}_3\text{P}/\text{CFC}$ directly used as the working electrode, bared carbon fiber cloth (CFC) as the counter electrode, and a Ag/AgCl reference electrode in an undivided H-type electrochemical cell. The electrochemical impedance spectroscopy (EIS) spectra of $\text{Ni}_2\text{P}/\text{CFC}$ and $\text{Cu}_3\text{P}/\text{CFC}$ were measured in 1.0 M KOH without and with 50 mM furfural electrolyte respectively employing an AC voltage with 10 mV amplitude over a frequency range of $100,000\text{--}1 \text{ Hz}$ and the applied

potential was -0.15 V vs. RHE.

For the two-electrode electrocatalysis system, $\text{Ni}_2\text{P}/\text{CFC}$ and $\text{Cu}_3\text{P}/\text{CFC}$ were separately employed as the anode and cathode. The potential range was cyclically scanned at a scan rate of 2.0 mV s^{-1} . Constant current experiment was conducted in an H-type electrochemical reactor with 20 mL of 1.0 M KOH solution with 50 mM furfural in each chamber in this two-electrode system ($\text{Ni}_2\text{P}/\text{CFC}$ as the anode and $\text{Cu}_3\text{P}/\text{CFC}$ as the cathode). The stability tests of $\text{Ni}_2\text{P}/\text{CFC}$ for simultaneous oxidation and hydrogenation of furfural in the two-electrode system were evaluated under constant current in a mixed solution with 1.0 M KOH and 50 mM furfural in each chamber of H-type cell for three successive cycles.

2.4. Product analysis

To quantitatively analyze the products of furfural hydrogenation and calculate the corresponding Faradaic efficiencies, 10 mL of the solution during chronoamperometry testing in the three-electrode configuration or constant current testing in the two-electrode configuration were evaporated by a rotary evaporator and then the evaporated products were dissolved in methanol, further analyzing by gas chromatography-mass spectrometry (GC-MS), and GC (Shimadzu), equipped with a FID. The carbon balance was examined in every test, which was found to be higher than 95%. The furfural oxidation products were quantified by nuclear magnetic resonance (NMR) spectrometer (Bruker Avance III 400 MHz).

The conversion (%) of furfural and the yield (%) of hydrogenation/oxidation products were calculated based on the following two equations:

$$\text{Conversion (\%)} = \frac{\text{mole of substrate consumed}}{\text{mole of initial substrate}} \times 100\% \quad (1)$$

$$\text{Yield (\%)} = \frac{\text{mole of product formed}}{\text{mole of initial substrate}} \times 100\% \quad (2)$$

The Faradaic efficiency (FE) of the formed product was calculated using the following equation:

$$\text{FE (\%)} = \frac{\text{mole of product formed}}{\text{total charge passed}/(n \times F)} \times 100\% \quad (3)$$

where n is the number of electron transfer for each product and F is the Faraday constant (96485 C mol^{-1}).

2.5. DFT calculations

All the calculations were performed within the framework of density function theory (DFT), using the Vienna Ab initio Simulation Package (VASP) with Perdew-Burke-Ernzerhof generalized gradient approximation (PBE-GGA) function [38,39]. The projector augmented wave (PAW) method was used to describe the inert core electrons. Both bulk Cu_3P and Ni_2P have hexagonal structure. We relaxed the structures until the total energy changes within $1 \times 10^{-5} \text{ eV}$ per atom and the Hellmann–Feynman force on each atomic site was less than 0.01 eV/\AA , with a 400 eV cutoff energy. $7 \times 7 \times 7$ and $9 \times 9 \times 11$ Monkhorst-Pack k-point sampling were respectively used for Cu_3P and Ni_2P . The optimized structures ($a = b = 6.979 \text{ \AA}$, $c = 7.198 \text{ \AA}$ for Cu_3P ; $a = b = 5.865 \text{ \AA}$, $c = 3.378 \text{ \AA}$ for Ni_2P) were in good agreement with the experimental values ($a = b = 6.959 \text{ \AA}$, $c = 7.143 \text{ \AA}$ for Cu_3P ; $a = b = 5.859 \text{ \AA}$, $c = 3.382 \text{ \AA}$ for Ni_2P). On the basis of the optimized unit cells, the six-layer 2×2 (1–10) surface and (001) surface were constructed for Cu_3P and Ni_2P , respectively. Accordingly, $2 \times 2 \times 1$ k-point sampling was used. The interactions of H with the surfaces were investigated at different coverages. In the calculations, the top four layers of the surfaces were allowed to relax together with adsorbates, while the bottom two layers were kept fixed to present the bulk properties.

Adsorption of H atom(s) on (1–10)- Cu_3P and (001)- Ni_2P surfaces

The hydrogen chemisorption energy (ΔE_{H}) could be used to describe the stability of hydrogen, which was obtained according to the following equation [40]:

$$\Delta E_{\text{H}} = 1/n\{E(\text{surf} + n\text{H}) - E(\text{surf}) - n/2E(\text{H}_2)\} \quad (4)$$

where n is the number of H atoms in the calculation.

The Gibbs free energy of the adsorbed state was calculated as the following equation [41]:

$$\Delta G_{\text{H}^*} = \Delta E_{\text{H}} + \Delta E_{\text{ZPE}} - T\Delta S_{\text{H}} \quad (5)$$

where ΔE_{H} is the hydrogen chemisorption energy, ΔE_{ZPE} is the difference in zero point energy between the adsorbed and gas state and ΔS_{H} is the entropy difference between the adsorbed and gas state.

3. Results and discussion

3.1. Structure and composition of $\text{Cu}_3\text{P/CFC}$ and $\text{Ni}_2\text{P/CFC}$

In this work, nanosheets structure Cu_3P and granular Ni_2P nanocrystals were directly grown on the commercial carbon fiber cloth (CFC) through a facile vapor-phase hydrothermal (VPH) method (Fig. 1a) [42]. From Fig. 1b, it can be clearly seen that the XRD patterns of the resulting gray-white CFC after phosphidation (Fig. S1, Supporting Information) confirm the transformation of Cu^{2+} (or Ni^{2+}) adsorbed on CFC to hexagonal crystal structure Cu_3P (or Ni_2P) grown on CFC. In details, the XRD peaks at $2\theta = 36.0^\circ$, 39.1° , 41.2° , 45.1° , 46.1° and 47.3° can be indexed to the (112), (202), (300), (211), (113) and (212) crystal faces of hexagonal Cu_3P (JCPDS no.01-071-2261), while the diffraction peaks at $2\theta = 40.8^\circ$, 44.6° , 47.3° , 54.2° , 54.9° , 66.2° , 72.6° and 74.8° can be attributed to the (111), (201), (210), (300), (211), (310), (311) and

(400) crystal faces of hexagonal Ni_2P (JCPDS no.00-003-0953). The low-magnification SEM images of $\text{Cu}_3\text{P/CFC}$ and $\text{Ni}_2\text{P/CFC}$ (Fig. S1, Supporting Information) indicate three-dimensional (3D) interlaced fiber framework of CFC can be maintained well with surface grown Cu_3P and Ni_2P nanostructures after VPH reaction. The high-magnification SEM image of $\text{Ni}_2\text{P/CFC}$ shows rough and granular morphology composed of numerous Ni_2P nanoparticles (Fig. 1c), in accordance with our previous work [34]. Furthermore, the TEM images were obtained to confirm the refined structure of Ni_2P grown on the CFC. As shown in Fig. 1d and the magnified TEM image (Fig. 1e), the Ni_2P nanoparticles are composed of more interconnected nanocrystals with very small crystal particle sizes of 2–12 nm. It is inferred that the small Ni_2P nanocrystals were firstly formed via a nanoscale Kirkendall pathway [43] under VPH conditions, further aggregating into secondary particles because of their extremely small dimensions and high surface energy. As shown in inset of Fig. 1d, an HRTEM image of an individual Ni_2P nanocrystal, exhibiting a interplanar spacing of 0.22 nm, which ascribed to the (111) plane of Ni_2P . However, the high-magnification SEM image (Fig. 1g) of $\text{Cu}_3\text{P/CFC}$ reveals a 3D hierarchical porous Cu_3P nanosheets structure evenly firmly anchored on the CFC, favourable for the accessibility of catalytic related active sites and the electron transfer, thereby enhancing the electrocatalytic activity [44,45]. Fig. 1h shows the TEM image of Cu_3P nanosheets, displaying an interplanar spacing of 0.25 nm (Fig. 1i), in consistent with the lattice spacing of Cu_3P (-1-12) plane. The SAED patterns (inset in Fig. 1h) further confirm this point [44], and demonstrate that the exposed surface of Cu_3P is the (1–10) plane. These results are consistent with the theoretical study that the (1–10) plane is the possible exposed surface for the Cu_3P , favourable for forming nanosheet structure [46]. Fig. 1f and j present their corresponding elemental mapping images of $\text{Ni}_2\text{P/CFC}$ and $\text{Cu}_3\text{P/CFC}$, respectively, indicating that both Cu/Ni and P are evenly distributed throughout the samples, further validating the formation of Ni_2P or Cu_3P on the CFC through VPH transformation of Ni^{2+} or Cu^{2+} -adsorbed CFC. Under the VPH conditions, the produced PH_3 gas from aqueous NaOH solution containing red phosphorus can react with the adsorbed Ni^{2+} or Cu^{2+} on the CFC to form Ni_2P or Cu_3P nanostructure film. And the energy-filtered TEM spectrum analysis demonstrates that the atomic ratio of Cu (or Ni) and P is close to 3:1 (or 2:1) (Fig. S2, Supporting Information), further verifying the formation of Cu_3P or Ni_2P on the CFC.

The surface XPS spectrum further verifies the existence of Cu or Ni element and P element in $\text{Cu}_3\text{P/CFC}$ or $\text{Ni}_2\text{P/CFC}$ (Fig. S3a, Supporting Information). Firstly, the P 2p and Cu 2p_{3/2} XPS spectra of Cu_3P nanosheets are shown in Fig. S3b and 3c (Supporting Information), it is clear that the peak at the binding energy of 933.2 eV could ascribe to Cu 2p_{3/2} spectra, and accompanying two peaks at 129.4 and 133.8 eV could ascribe to P 2p spectra. The peaks at 933.2 and 129.4 eV are close to the binding energies for Cu and P in Cu_3P , and the peak at 133.8 eV for P can be attributed to the oxidized P species deriving from an oxidation reaction between the surface of Cu_3P and the oxygen came from air contact [45,47]. Similarly, the fitting three peaks of high-resolution Ni 2p_{3/2} XPS spectrum (Fig. S3b, Supporting Information) are corresponding to $\text{Ni}\delta^+$ species, oxidized Ni species, and the satellite peak of Ni 2p_{3/2} in Ni_2P , respectively [20,48]. Those high-resolution XPS spectrums are consistent with the previous reports [49,50], illustrating the Cu or Ni possess a partial positive charge while the P has a partial negative charge [49,50], thus proving a charge shift from Ni or Cu element to P element in Cu_3P or Ni_2P .

3.2. Electrocatalytic furfural hydrogenation reaction (FHR)

Generally, the hydrogenation products of furfural mainly include 2-methylfuran (2-MF), furfuryl alcohol (FAL), tetrahydrofurfuryl alcohol (THFA) and tetrahydromethylfuran (THMF), as shown in Fig. S4 (Supporting Information) [3]. In this work, the conversion products, Faradaic efficiency and reaction rate of the prepared transition metal

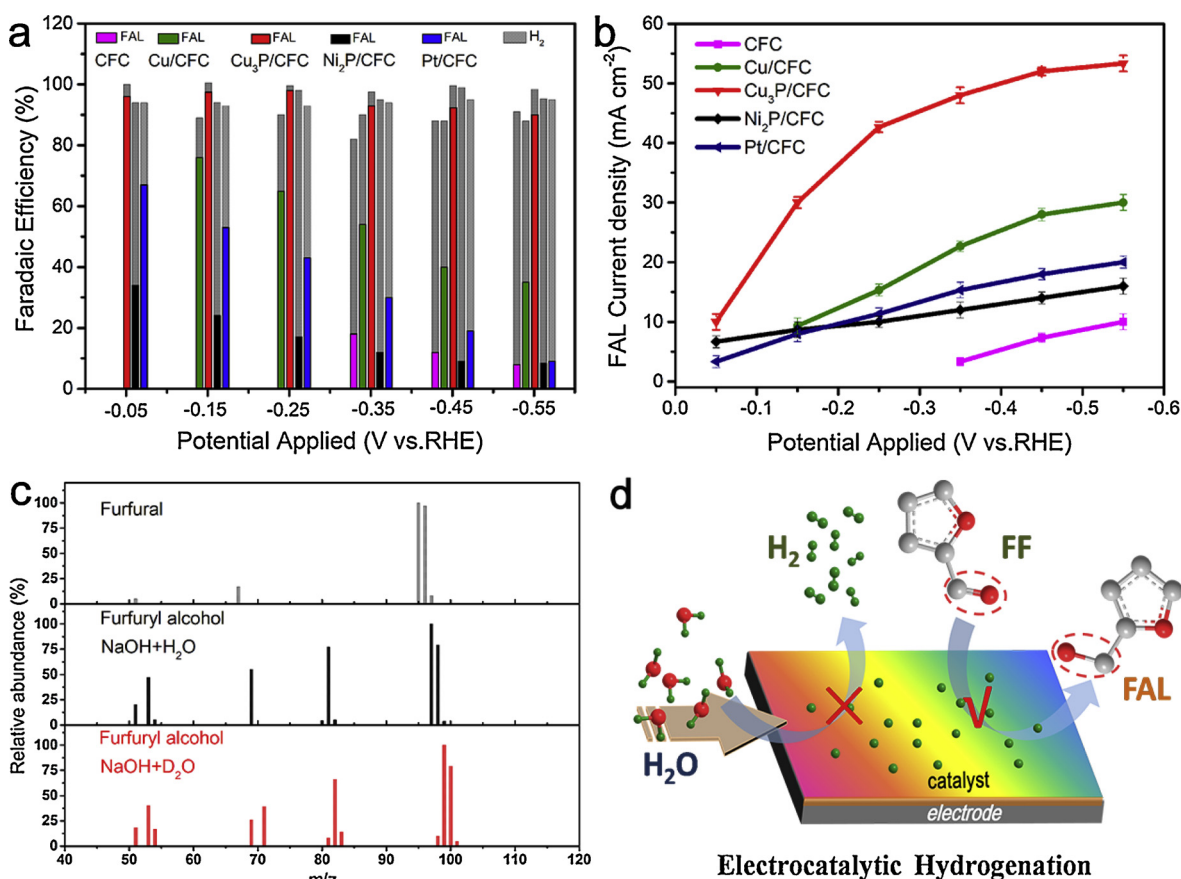


Fig. 2. The electrolysis of furfural over different electrodes: (a) the FAL and H₂ Faradaic efficiency, (b) the FAL partial current density at different applied potential measured in N₂-saturated 1 M KOH solution with 50 mM furfural in the working electrode reaction tank. (c) Mass spectra of furfural and its products (FAL) obtained in H₂O/NaOH and D₂O/NaOH. (d) The schematics illustrating the electrocatalytic FHR and HER at catalyst surface.

phosphides/CFC electrodes towards electrocatalytic furfural hydrogenation reaction (FHR) were firstly evaluated by controlled-potential electrolysis in a typical three-electrode system (Fig. S5, Supporting Information) using an H-type separated reactor (1.0 M KOH electrolyte with 50 mM furfural in working electrode reaction compartment, and 1.0 M KOH electrolyte in counter electrode reaction compartment). For obtaining a meaningful comparison, the Cu/CFC, Pt/CFC and CFC electrodes were also evaluated under the identical experimental process. In 1.0 M KOH containing 50 mM furfural solution, the pure CFC electrode shows very poor FHR performance, displayed of an onset potential of about -0.35 V (vs. RHE) for FHR, a maximum FAL Faradaic efficiency of 18% and low current density at even high overpotentials, demonstrating that the bare CFC possesses inferior FHR selectivity and activity. The Cu₃P/CFC electrode exhibits significantly enhanced FAL Faradaic efficiency and decreased onset potential for FHR compared with the bare CFC electrode, as shown in Fig. 2a. In particular, the FAL Faradaic efficiencies over Cu₃P/CFC electrode exceed 95% in the potential range of -0.05 to -0.55 V (vs. RHE), implying the severely inhibited HER, while the Ni₂P/CFC electrode exhibits ~40% Faradaic efficiency for FHR at -0.05 V (vs. RHE), moreover decreases sharply with increasing the overpotentials, demonstrating that the HER is still a strong competitive reaction. For comparison, the Cu/CFC and Pt/CFC were also used to catalyze the FHR, and FAL was generated over Cu/CFC electrode at -0.15 V (vs. RHE) with a Faradaic efficiency of 75% and Pt/CFC electrode with excellent HER activity shows 65% Faradaic efficiency for FHR, moreover decreases sharply with further increasing the overpotentials similarly to Ni₂P/CFC electrode. Fig. 2b exhibits the dependence of the FAL current density on the applied potential. Ni₂P/CFC and Pt/CFC electrodes all indicate low FAL current density (5–20 mA cm⁻² over the potential range from -0.05 to -0.55 V vs.

RHE), probably due to a strong HER competition on these two electrodes. The Cu/CFC electrode presents a moderate FAL current density (10–30 mA cm⁻² over the potential range from -0.05 to -0.55 V vs. RHE), delivering high selective hydrogenation activity of furfural [51]. More importantly, the Cu₃P/CFC electrode shows a higher FAL current density, which increases with the applied potential and reaches 55 mA cm⁻² at -0.55 V (vs. RHE). Undoubtedly, the Cu₃P/CFC electrode exhibits the highest selectivity (~100%) for converting furfural to furfuryl alcohol compared to other electrodes at -0.35 V (vs. RHE) at a moderate overall current density, as shown in Fig. S6 (Supporting Information). All those experimental results demonstrate that the Cu₃P/CFC electrode possesses high Faradaic efficiency, large current density and high selectivity of furfural to furfuryl alcohol.

In order to understand the catalytic transfer hydrogenation process using H₂O as hydrogen source on Cu₃P/CFC electrode for furfural electrocatalytic hydrogenation process, we performed an isotopic labeling study using D₂O/NaOH as electrolyte. As shown in Fig. 2c, utilizing D₂O to replace H₂O, the molecular mass of the formed FAL (*m/z* = 100 with 2D atoms) product is obviously increased compared with the standard mass spectra of FAL (*m/z* = 98) and the substrate furfural (*m/z* = 96), which unambiguously demonstrates that the hydrogen source for furfural hydrogenation product is originated from water in electrolyte. Therefore, the possible pathway of the efficient FHR over Cu₃P/CFC may be depicted in Fig. 2d. Firstly, driven by the electric potential, water splitting occurs at the surface of catalyst to form active hydrogen atoms, namely, the Volmer reaction process, which is key step for both HER and electrocatalytic hydrogenation of organics. Subsequently, the adsorbed active hydrogen (H_{ads}) on the catalyst surface selectively reacts with an adsorbed furfural molecular to form FAL, effectively inhibiting the H₂ production through the Heyrovsky or Tafel

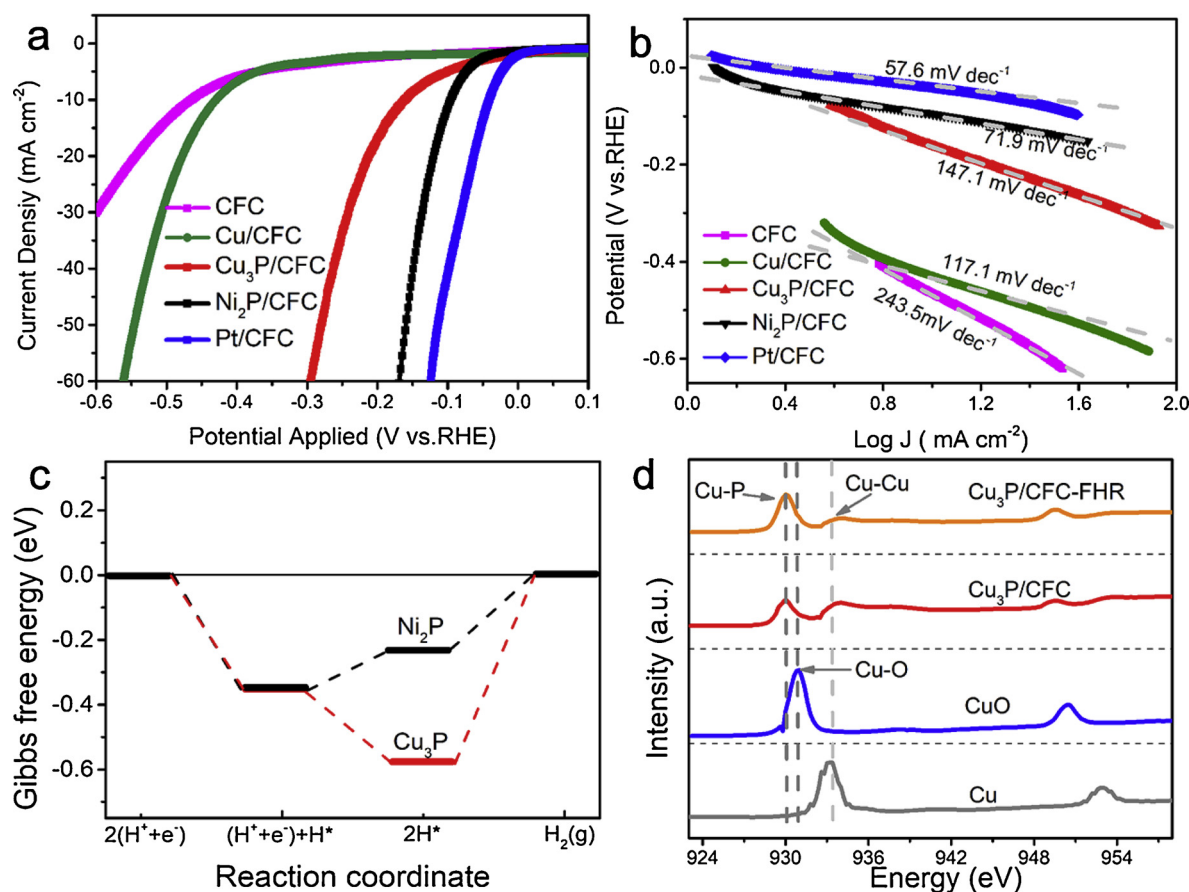


Fig. 3. (a) HER polarization curves of Pt/CFC, Ni₂P/CFC, Cu₃P/CFC, Cu/CFC and CFC, (b) Tafel plots of Pt/CFC, Ni₂P/CFC, Cu₃P/CFC, Cu/CFC and CFC calculated from Fig. 3a. (c) Calculated energy changes for the HER on the Cu₃P (1–10), Ni₂P (001) surfaces. The energy change for the 2(H⁺ + e⁻) to H₂ reaction is defined as zero by setting the reference potential to that of the standard hydrogen electrode. (d) The Cu L_{3,2}-edge XAS spectra of Cu, CuO, Cu₃P/CFC and Cu₃P/CFC-FHR.

process. Our experimental results demonstrate that an efficient electrocatalyst for the hydrogenation reaction of organics must be able to effectively stabilizing and utilizing the active hydrogen (H_{ads}) from water splitting on the catalysts surface, but not for high HER activity.

For the electrocatalytic conversion of furfural in an aqueous electrolyte, HER process is the major competitive reaction [20,23], therefore the HER activities of the as-prepared electrocatalysts were also evaluated in 1.0 M KOH electrolyte. As shown in Fig. 3a, the onset potentials are -0.35, -0.32, -0.052, -0.05 and -0.015 V (vs. RHE) and the Tafel slopes are 243.5, 117.1, 147.1, 71.9 and 57.6 mV dec⁻¹ for CFC, Cu/CFC, Cu₃P/CFC, Ni₂P/CFC and Pt/CFC electrodes, respectively (Fig. 3b). Apparently, the Cu₃P/CFC electrode possesses the onset potential approximate to the Ni₂P/CFC and Pt/CFC, demonstrating its excellent HER activity (Volmer reaction process), however, its Tafel slope of 147.1 mV dec⁻¹ is much larger than that of Ni₂P/CFC and Pt/CFC, indicating its sluggish Tafel reaction kinetics for H₂ generation. This means that the produced active hydrogen (H_{ads}) from water splitting on the Cu₃P/CFC surface may be effectively utilized for the furfural hydrogenation reaction. In this work, we also performed the electrochemical impedance spectroscopy (EIS) analysis of Cu₃P/CFC and Ni₂P/CFC in 1.0 M KOH solution without and with furfural. As shown in Fig. S7 (Supporting Information), the greatly reduced *R*_{ct} value in the presence of furfural for Cu₃P/CFC demonstrates that the furfural hydrogenation reaction is more kinetically favourable in comparison with the HER without furfural in 1.0 KOH solution, while the very close *R*_{ct} value of Ni₂P/CFC in the presence and absence of furfural in 1.0 KOH electrolyte indicates its strong HER competitive reaction. The EIS results further confirm that the Cu₃P/CFC can effectively utilize the active hydrogen (H_{ads}) from water splitting through the Volmer process, thus

enhancing the furfural hydrogenation conversion performance.

To gain deep insight into the competitive mechanism between FHR and HER process over the Cu₃P/CFC and Ni₂P/CFC electrodes, DFT calculations were also carried out in this study. The hydrogen adsorption free energy (ΔG_H) has been widely accepted as a descriptor of HER activity for various electrocatalysts [41,52]. The calculations results demonstrate that the ΔG_H values of Ni₂P and Cu₃P are -0.23 eV and -0.34 eV respectively, indicating more superior HER activity of Ni₂P (Fig. 3c), consistent with the experimental results. For the atomic hydrogen, our calculations results (Fig. S8a, b, Supporting Information) suggest that the 3-coordinated Cu/Ni hollow sites are highly preferred on (1–10)-Cu₃P/(001)-Ni₂P. The adsorption energies at different coverage were calculated for the Cu₃P and Ni₂P, as shown in Table S2 (Supporting Information). Obviously, the adsorption energy of the first atomic hydrogen is -0.58 eV for the Cu₃P, the same with the Ni₂P. On the Cu₃P surface, there are two available hollow sites, the additional atomic hydrogen therefore decreases the adsorption energy to -0.82 eV. However, there is only one hollow site on the Ni₂P surface, the second atomic hydrogen has to interact with the less active Ni-P bridge site, which is an heat absorbing process, thus resulting in an adsorption energy of -0.47 eV. Consequently, the desorption of H₂ becomes less energy-consuming on the Ni₂P [53]. Our calculations results demonstrate that the superior furfural hydrogenation activity on the Cu₃P/CFC should be attributed to higher active hydrogen concentration on the Cu₃P surface and larger H₂ desorption energy, which effectively inhibits the H₂ generation, thus greatly improving the furfural hydrogenation efficiency.

After the furfural hydrogenation reaction (FHR), the XPS and SEM characterizations were used to interrogate the chemical composition

and structure information of used $\text{Cu}_3\text{P/CFC}$ (named as $\text{Cu}_3\text{P/CFC-FHR}$). The characterization results demonstrate that the composition and structure of the $\text{Cu}_3\text{P/CFC}$ have no significant change after the FHR (Fig. S3 and Fig. S9, Supporting Information), indicating its high applicable stability. Further, the Cu $L_{3,2}$ -edge X-ray absorption spectra (XAS) of electrode and corresponding reference standard materials (Fig. 3d) indicate that the Cu_3P on the CFC is composed of Cu-Cu and Cu-P bonds [54], compared with Cu/CFC with only Cu-Cu bond. After the FHR, no new Cu-related bonds can be observed, further indicating its high stability, consistent with the SEM and XPS characterization results. In general, the furfural adsorption energy on the surface of Cu-based catalysts is calculated through a η_1 -(O)-aldehyde configuration (perpendicular configuration), which contributes to selective hydrogenation of furfural to FAL [15,51]. Therefore, considering superior furfural electrocatalytic hydrogenation activity of the $\text{Cu}_3\text{P/CFC}$ electrode than Cu/CFC electrode, it is reasonable to suggest that the superior FHR activity should be mainly originated from the Cu-P component of Cu_3P structure.

3.3. Electrocatalytic furfural oxidation reaction (FOR)

The electrochemical performances of the $\text{Ni}_2\text{P/CFC}$ and $\text{Cu}_3\text{P/CFC}$ toward furfural oxidation reaction (FOR) were subsequently evaluated in 1.0 M KOH electrolyte with a three-electrode system. For the electrocatalytic oxidation of furfural in an aqueous electrolyte, water oxidation is the major competitive reaction. Therefore, the as-prepared $\text{Ni}_2\text{P/CFC}$ and $\text{Cu}_3\text{P/CFC}$ electrodes were firstly investigated by the linear sweep voltammetry (LSV) in 1.0 M KOH solution for evaluating their OER activities. As shown in Fig. 4a and Fig. S10 (Supporting

Information), both $\text{Ni}_2\text{P/CFC}$ and $\text{Cu}_3\text{P/CFC}$ present excellent OER catalytic behavior, similar to the previously reported transition metal phosphides [44,48]. In detail, the polarization curves of the $\text{Cu}_3\text{P/CFC}$ and $\text{Ni}_2\text{P/CFC}$ demonstrate the overpotentials of 350 mV and 290 mV for OER, respectively. Significantly, after the introduction of 50 mM furfural into 1.0 M KOH electrolyte, the steady-state LSV curves shift toward negative potential direction, implying the furfural oxidation happened at both $\text{Cu}_3\text{P/CFC}$ and $\text{Ni}_2\text{P/CFC}$. As the anode, the potentials at current density of 10 mA cm^{-2} of $\text{Ni}_2\text{P/CFC}$ and $\text{Cu}_3\text{P/CFC}$ shift to $\sim 1.34 \text{ V}$ and 1.43 V (vs. RHE), respectively (Fig. 4a), and the rapid increase in the current density can be obviously observed within 1.40 V (vs. RHE) for $\text{Ni}_2\text{P/CFC}$ electrode, where the OER does not happen, illustrative of more favorable furfural oxidation than OER for both $\text{Ni}_2\text{P/CFC}$ and $\text{Cu}_3\text{P/CFC}$. In detail, the overpotentials for the furfural oxidation reaction (FOR) are at least 160 mV and 130 mV much lower than that of OER for the $\text{Ni}_2\text{P/CFC}$ and $\text{Cu}_3\text{P/CFC}$ (Fig. 4a), respectively, indicating more superior FOR activity of the $\text{Ni}_2\text{P/CFC}$ compared to the $\text{Cu}_3\text{P/CFC}$.

In order to deeply investigate the FOR activities of these two electrodes, the chronoamperometry experiments carried out at different potentials for the furfural oxidation demonstrate that these two electrodes can convert furfural to corresponding high-value product of furoic acid (FA) with high Faradaic efficiency (exceeding 85% over the potential range of 1.2–1.7 V vs. RHE) for both $\text{Cu}_3\text{P/CFC}$ and $\text{Ni}_2\text{P/CFC}$ (Fig. 4b). Not surprisingly, the $\text{Ni}_2\text{P/CFC}$ electrode shows lower onset potential and higher current density for the FOR compared to the $\text{Cu}_3\text{P/CFC}$, and the current density of the both furfural oxidation on the $\text{Ni}_2\text{P/CFC}$ increases with the applied potential, capable of reaching 78 mA cm^{-2} at 1.7 V (vs. RHE) achieved $\sim 90\%$ Faradaic efficiency (Fig. 4c), further indicating the superior FOR activity of the $\text{Ni}_2\text{P/CFC}$.

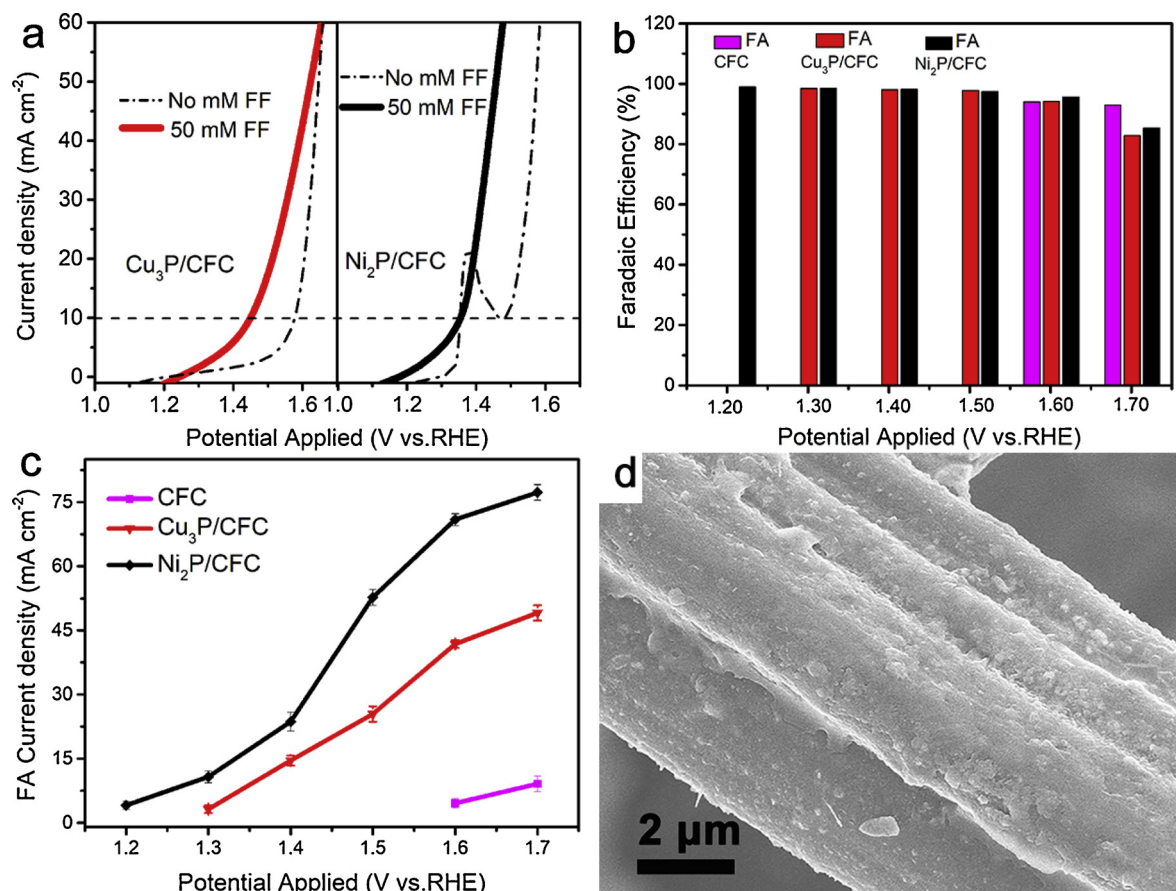


Fig. 4. (a) The polarization curves of $\text{Ni}_2\text{P/CFC}$ and $\text{Cu}_3\text{P/CFC}$ at a scan rate of 5 mV s^{-1} in 1.0 M KOH with and without 50 mM furfural. The electrolysis of furfural over different electrodes: (b) the FA Faradaic efficiency, (c) the FA partial current density at different applied potential measured in N_2 -saturated 1.0 M KOH solution with 50 mM furfural in the working electrode reaction tank. (d) SEM image of $\text{Ni}_2\text{P/CFC-FOR}$.

It has been widely accepted that the OER activity of the transition metal (Fe, Co, Ni) based electrocatalysts is mainly ascribed from the electrochemical transformed high valence state transition metal species in alkaline electrolyte under anodic potentials [55–57]. Therefore, we also investigated the change of the structure and composition of the Ni₂P/CFC after the FOR (denoted as Ni₂P/CFC-FOR). Firstly, the cyclic voltammetry (CV) measurements of Cu₃P/CFC and Ni₂P/CFC electrodes were performed in 1.0 M KOH solution with and without 50 mM furfural at a scan rate of 20 mV s⁻¹. As shown in Fig. S11a (Supporting Information), it can be clearly seen that the onset potential of FOR for Ni₂P/CFC is almost identical with the potential of the oxidation of Ni species in Ni₂P to high valence Ni species, possibly meaning the high valence state Ni species are the active sites for FOR. Comparatively, Cu component in Cu₃P was oxidized to high valence state at a lower potential, where FOR has not happened (Fig. S11b, Supporting Information). Secondly, the surface survey XPS spectrum shows that the Ni and P elements are still dominant of the Ni₂P/CFC-FOR (Fig. S3a, Supporting Information). The high resolution XPS spectrum of Ni 2p (Fig. S3b, Supporting Information) indicates that the peak at binding energy of 853.8 eV assigned to Niδ⁺ of Ni₂P is disappeared and an enhancement of the peak at the binding energy of 856.3 eV corresponding to oxidized Ni species can be clearly observed, suggesting the formation of high valence state Ni species for the Ni₂P/CFC-FOR. This oxidation phenomenon can be also further proved by the enhanced intensity of the XPS peak stemmed from the oxidized P species (Fig. S3c, Supporting Information). Thirdly, the SEM image (Fig. 4d and Fig. S12) of the Ni₂P/CFC-FOR also verifies that the morphology of the Ni₂P/CFC after the FOR is obviously changed from the surface nanoparticle structure to compacted film structure, which was further proved by TEM characterization (Fig. S13a, Supporting Information), showing that an amorphous nano-thin layer is formed around the Ni₂P nanoparticles after FOR. Significantly, the XRD patterns of Ni₂P/CFC-FOR (Fig. S13b, Supporting Information) exhibit new crystal phases possibly attributed to Ni oxy/hydroxide phase after FOR. Collectively, it is reasonable to suggest that the catalytic active sites of Ni₂P/CFC for the FOR should be originated from high valence state Ni species (such as oxides/hydroxides and oxyhydroxides), consistent with the reported results [58,59].

3.4. Simultaneous furfural oxidation and hydrogenation reactions

Although the as-prepared Ni₂P/CFC and Cu₃P/CFC all exhibit the catalytic performances for both furfural oxidation reaction (FOR) and furfural hydrogenation reaction (FHR), the Ni₂P/CFC is more favourable for the FOR and the Cu₃P/CFC is more favourable for the FHR. Therefore, we can integrate the Ni₂P/CFC as the anode and Cu₃P/CFC as the cathode for simultaneous oxidation and hydrogenation reduction of furfural to generate high value-added furfural derived products. Therefore, a two-electrode H-type electrochemical cell with Nafion membrane as separator was used as the reactor using the Ni₂P/CFC as the anode and the Cu₃P/CFC as the cathode. The electrolyte is 1.0 M KOH solution with 50 mM furfural. And, the Nafion membrane can effectively prevent the furfuryl alcohol penetrating through the membrane into the anode compartment, assuring the electrocatalytic oxidation of furfural on the Ni₂P/CFC and electrocatalytic hydrogenation reduction of furfural on the Cu₃P/CFC, as shown in Fig. S14 (Supporting Information). This H-type reaction device also provides a novel route to combine the anodic and cathodic reactions for simultaneously producing high value furanic compounds (Fig. 5a). Such an integrated two-electrode system composed of the Ni₂P/CFC anode and the Cu₃P/CFC cathode exhibits the lowest cell voltage to power the furfural conversion among different two-electrode configuration systems (Fig. S15, Supporting Information). In detail, the LSV curves (Fig. 5b) of the Ni₂P/CFC and Cu₃P/CFC coupling system in 1.0 M KOH solution displays an starting voltage at ~1.55 V for whole water splitting and the cell voltage arrives at 1.67 V to achieve a current density of 10 mA cm⁻² in the absence of furfural. However, the addition of 50 mM

furfural in the electrolyte, the onset voltage of electrolysis is obviously decreased to ~1.2 V and the cell voltage at 10 mA cm⁻² needs only ~1.40 V, implying more superior oxidation and hydrogenation performance toward electrocatalytic conversion of furfural using this two-electrode integrated system in comparison with the overall water splitting.

In order to gain deeper understanding into the electrocatalytic conversion process of furfural, constant current (20 mA) experiment was conducted in such two-electrode H-type reactor with 20 mL of 1.0 M KOH containing 50 mM furfural in each chamber, and the furfural conversion products were analyzed by the NMR and GC techniques (Figs. S16 and S17, Supporting Information). Fig. S16 shows the GC results of furfural and its electrocatalytic hydrogenation product (furfuryl alcohol, FAL) during the electrocatalysis. Similarly, it exhibits the increase of FAL along with the decrease of furfural as the reaction goes on, demonstrating the successful conversion of furfural to FAL. After the reaction of 160 min, the GC signal of furfural apparently disappears but that of FAL obviously increases to the maximum value, indicating a complete conversion of furfural. Fig. S17 shows the ¹H NMR results of the furfural and its oxidation product (furoic acid, FA) during the electrocatalysis. It apparently exhibits the increase of FA along with the decrease of furfural over reaction time, illustrating the successful transformation from furfural to FA. In all reactions, the applied voltage is ~1.4 V, delivering a current density of 10 mA cm⁻². Under such an applied voltage, water splitting reaction is hardly happened, thus resulting in a nearly 100% Faradaic efficiency for furfural electrocatalytic oxidation upgrading [59]. And the furfural conversion and the FAL and FA yields with reaction time are plotted in Fig. 5c, and the Faradaic efficiencies of 97–99% for the furfural conversion can be observed. To evaluate the durability of the catalyst, three consecutive cycles of the constant voltage mode electrocatalysis by using the Ni₂P/CFC and Cu₃P/CFC coupling configuration were performed in this work. Significantly, Fig. 5d shows the calculated Faradaic efficiencies for FAL and FA production consistently range between 95–99%, demonstrating the robust stability of this two-electrode integrated system for the electrocatalytic furfural conversion.

4. Conclusion

The self-supported nanostructure transition metal phosphides on the commercial carbon fiber cloth (Cu₃P/CFC or Ni₂P/CFC) were fabricated through a vapor-phase hydrothermal route. The furfural electrocatalytic conversion system was designed and constructed by using water as the hydrogen source in a membrane separated H-type reactor, catalyzed by Ni₂P/CFC anode and Cu₃P/CFC cathode. As a result, the Cu₃P/CFC electrode demonstrated high Faradaic efficiency, large current density and selective electrocatalytic conversion of furfural to furfuryl alcohol (FAL), while the Ni₂P/CFC electrode showed more superior furfural oxidation activity, effectively conversion of furfural to furoic acid (FA) with high FE and selectivity. The DFT calculations revealed that the excellent furfural electrocatalytic hydrogenation activity on the Cu₃P/CFC could be attributed to higher concentration H_{ads} on the catalyst surface, favourable for the furfural hydrogenation reaction with high Faradaic efficiency, compared to the Ni₂P/CFC. The superior furfural oxidation activity of the Ni₂P/CFC was mainly stemmed from the formed high valence state active Ni species. The concept developed in this work can be extensive for simultaneously electrocatalytic hydrogenation and oxidation to produce high value-added products from other biomass reactant using the low-cost and abundant transitional metal based electrocatalysts.

Acknowledgments

This work was financially supported by the CAS Pioneer Hundred Talents Program, the Natural Science Foundation of China (Grant No. 51672277 and 51432009), and the CAS/SAFEA International

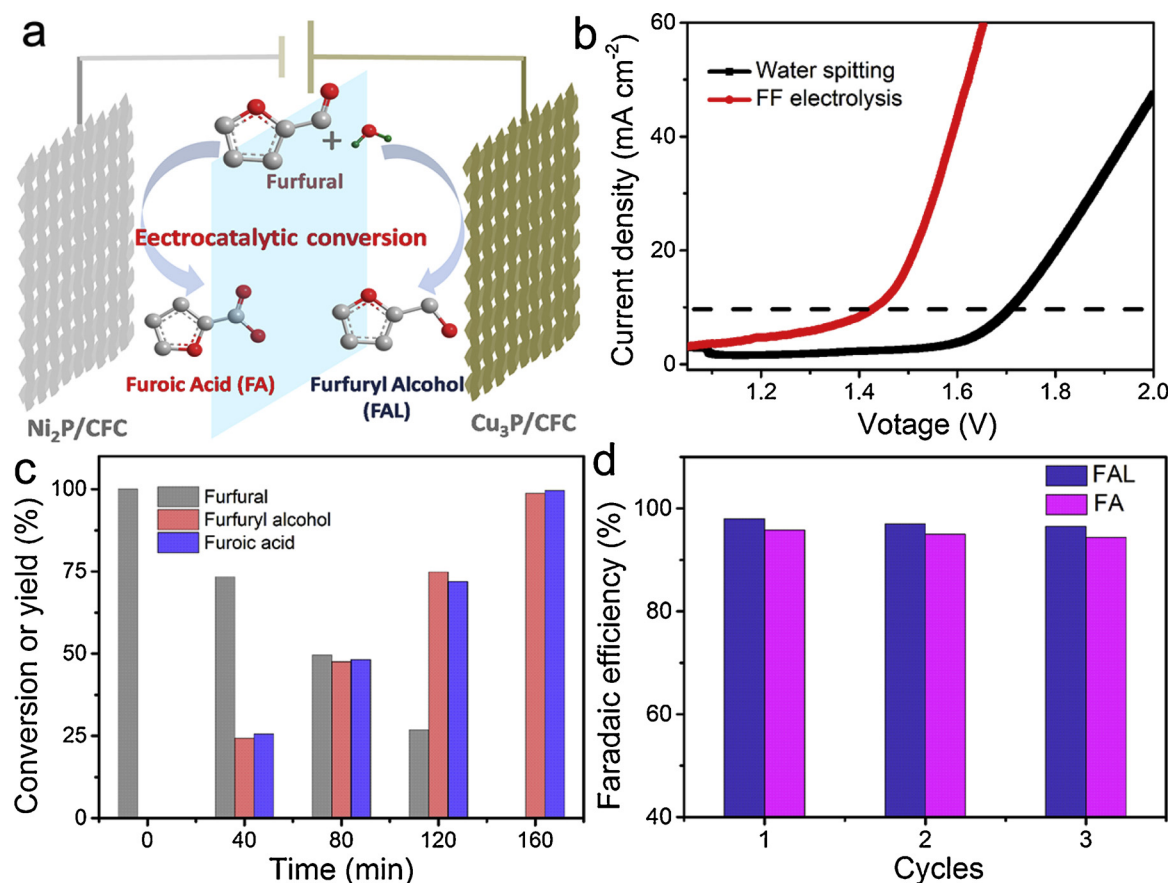


Fig. 5. (a) Schematic diagram of $\text{Cu}_3\text{P/CFC}$ and $\text{Ni}_2\text{P/CFC}$ for two-electrode electrocatalytic conversion of furfural. (b) LSV plots without iR compensation of $\text{Cu}_3\text{P/CFC}$ (as cathode) and $\text{Ni}_2\text{P/CFC}$ (as anode) two-electrode system in 1.0 M KOH without and with 50 mM furfural. (c) Conversion and yield (%) changes of furfural and its oxidation/hydrogenation products. (d) Faradaic efficiencies of $\text{Cu}_3\text{P/CFC}$ (cathode) and $\text{Ni}_2\text{P/CFC}$ (anode) for FAL and FA production under three successive electrolysis cycles.

Partnership Program for Creative Research Teams of Chinese Academy of Sciences, China.

Appendix A. Supplementary data

Supplementary material related to this article can be found, in the online version, at doi:<https://doi.org/10.1016/j.apcatb.2018.12.025>.

References

- J.S. Luterbacher, J.M. Rand, D.M. Alonso, J. Han, J.T. Youngquist, C.T. Maravelias, B.F. Pfleger, J.A. Dumesic, *Science* 343 (2014) 277–280.
- G.-H. Wang, J. Hilgert, F.H. Richter, F. Wang, H.-J. Bongard, B. Spliethoff, C. Weidenthaler, F. Schüth, *Nat. Mater.* 13 (2014) 293–300.
- Y. Kwon, K.J.P. Schouten, J.C. van der Waal, E. de Jong, M.T.M. Koper, *ACS Catal.* 6 (2016) 6704–6717.
- J.J. Roylance, T.W. Kim, K.-S. Choi, *ACS Catal.* 6 (2016) 1840–1847.
- C.O. Tuck, E. Pérez, I.T. Horváth, R.A. Sheldon, M. Poliakoff, *Science* 337 (2012) 695–699.
- L.D. Schmidt, P.J. Dauenhauer, *Nature* 447 (2007) 914–915.
- Z. Lin, W. Wan, S. Yao, J.G. Chen, *Appl. Catal. B. Environ.* 233 (2018) 160–166.
- Z. Gao, C. Li, G. Fan, L. Yang, F. Li, *Appl. Catal. B. Environ.* 226 (2018) 523–533.
- J. Wu, G. Gao, J. Li, P. Sun, X. Long, F. Li, *Appl. Catal. B. Environ.* 203 (2017) 227–236.
- Y. Nakagawa, M. Tamura, K. Tomishige, *ACS Catal.* 3 (2013) 2655–2668.
- Y. Wang, G. Ding, X. Yang, H. Zheng, Y. Zhu, Y. Li, *Appl. Catal. B. Environ.* 235 (2018) 150–157.
- R. Alamillo, M. Tucker, M. Chia, Y. Pagan-Torres, J. Dumesic, *Green Chem.* 14 (2012) 1413–1419.
- W. Gong, C. Chen, Y. Zhang, H. Zhou, H. Wang, H. Zhang, Y. Zhang, G. Wang, H. Zhao, *ACS Sustain. Chem. Eng.* 5 (2017) 2172–2180.
- M. Besson, P. Gallezot, C. Pinel, *Chem. Rev.* 114 (2014) 1827–1870.
- J.J. Bozell, G.R. Petersen, *Green Chem.* 12 (2010) 539–554.
- A. Villa, M. Schiavoni, S. Campisi, G.M. Veith, L. Prati, *ChemSusChem* 6 (2013) 609–612.
- S.E. Davis, L.R. Houk, E.C. Tamargo, A.K. Datye, R.J. Davis, *Catal. Today* 160 (2011) 55–60.
- M. Hronec, K. Fulajtárová, I. Vávra, T. Soták, E. Dobročka, M. Mičušik, *Appl. Catal. B. Environ.* 181 (2016) 210–219.
- M.J. Taylor, L.J. Durndell, M.A. Isaacs, C.M.A. Parlett, K. Wilson, A.F. Lee, G. Kyriakou, *Appl. Catal. B. Environ.* 180 (2016) 580–585.
- B. You, N. Jiang, X. Liu, Y. Sun, *Angew. Chem. Int. Ed.* 55 (2016) 9913–9917.
- P. Nilges, U. Schröder, *Energy Environ. Sci.* 6 (2013) 2925–2931.
- J.J. Roylance, K.-S. Choi, *Green Chem.* 18 (2016) 2956–2960.
- H.G. Cha, K.-S. Choi, *Nat. Chem.* 7 (2015) 328–333.
- Z.W. Seh, J. Kibsgaard, C.F. Dickens, I.B. Chorkendorff, J.K. Norskov, T.F. Jaramillo, *Science* 355 (2017) 146–158.
- S. Xu, P. Zhou, Z. Zhang, C. Yang, B. Zhang, K. Deng, S. Bottle, H. Zhu, *J. Am. Chem. Soc.* 139 (2017) 14775–14782.
- H. Li, F. Qin, Z. Yang, X. Cui, J. Wang, L. Zhang, *J. Am. Chem. Soc.* 139 (2017) 3513–3521.
- S.-H. Ye, J.-X. Feng, G.-R. Li, *ACS Catal.* 6 (2016) 7962–7969.
- D.D. Zhu, J.L. Liu, S.Z. Qiao, *Adv. Mater.* 28 (2016) 3423–3452.
- M. Li, N. Zhang, R. Long, W. Ye, C. Wang, Y. Xiong, *Small* 13 (2017) 1604173–1604179.
- X.H. Chadderdon, D.J. Chadderdon, J.E. Matthiesen, Y. Qiu, J.M. Carraher, J.-P. Tessonnier, W. Li, *J. Am. Chem. Soc.* 139 (2017) 14120–14128.
- C. Yan, H. Li, Y. Ye, H. Wu, F. Cai, R. Si, J. Xiao, S. Miao, S. Xie, F. Yang, Y. Li, G. Wang, X. Bao, *Energy Environ. Sci.* 11 (2018) 1204–1210.
- K.J. Carroll, T. Burger, L. Langenegger, S. Chavez, S.T. Hunt, Y. Román-Leshkov, F.R. Brushett, *ChemSusChem* 9 (2016) 1904–1910.
- L. Liu, H. Liu, W. Huang, Y. He, W. Zhang, C. Wang, H. Lin, *J. Electroanal. Chem.* 804 (2017) 248–253.
- X. Zhang, Y. Liu, Q. Xiong, G. Liu, C. Zhao, G. Wang, Y. Zhang, H. Zhang, H. Zhao, *Electrochim. Acta* 254 (2017) 44–49.
- G. Chamoulaud, D. Floner, C. Moinet, C. Lamy, E.M. Belgsir, *Electrochim. Acta* 46 (2001) 2757–2760.
- C. Tang, R. Zhang, W. Lu, Z. Wang, D. Liu, S. Hao, G. Du, A.M. Asiri, X. Sun, *Angew. Chem. Int. Ed.* 55 (2016) 1–6.
- N. Jiang, B. You, R. Boonstra, I.M. Terrero Rodriguez, Y. Sun, *ACS Energy Lett.* 1 (2016) 386–390.

- [38] J.P. Perdew, K. Burke, M. Ernzerhof, *Phys. Rev. Lett.* 77 (1996) 3865–3868.
- [39] G. Kresse, D. Joubert, *Phys. Rev. B* 59 (1999) 1758–1775.
- [40] B. Hinnemann, P.G. Moses, J. Bonde, K.P. Jørgensen, J.H. Nielsen, S. Hørch, I. Chorkendorff, J.K. Nørskov, *J. Am. Chem. Soc.* 127 (2005) 5308–5309.
- [41] J.K. Nørskov, T. Bligaard, A. Logadottir, J.R. Kitchin, J.G. Chen, S. Pandalov, J.K. Nørskov, *J. Electrochem. Soc.* 152 (2005) J23–J26.
- [42] P. Liu, H. Zhang, H. Liu, Y. Wang, X. Yao, G. Zhu, S. Zhang, H. Zhao, *J. Am. Chem. Soc.* 133 (2011) 19032–19035.
- [43] Z. Zhang, G. Yu, H. Li, J. Liu, X. Huang, W. Chen, *Phys. Chem. Chem. Phys.* 20 (2018) 10407–10417.
- [44] A. Han, H. Zhang, R. Yuan, H. Ji, P. Du, *ACS Appl. Mater. Interfaces* 9 (2017) 2240–2248.
- [45] J. Tian, Q. Liu, N. Cheng, A.M. Asiri, X. Sun, *Angew. Chem. Int. Ed.* 53 (2014) 9577–9581.
- [46] E.J. Popczun, J.R. McKone, C.G. Read, A.J. Biacchi, A.M. Wilttrout, N.S. Lewis, R.E. Schaak, *J. Am. Chem. Soc.* 135 (2013) 9267–9270.
- [47] H. Pfeiffer, F. Tancrèt, T. Brousse, *Electrochim. Acta* 50 (2005) 4763–4770.
- [48] B. You, N. Jiang, M. Sheng, M.W. Bhushan, Y. Sun, *ACS Catal.* 6 (2016) 714–721.
- [49] Z. Xing, Q. Liu, A.M. Asiri, X. Sun, *Adv. Mater.* 26 (2014) 5702–5707.
- [50] J. Tian, Q. Liu, A.M. Asiri, X. Sun, *J. Am. Chem. Soc.* 136 (2014) 7587–7590.
- [51] S. Sittitha, T. Sooknoi, Y. Ma, P.B. Balbuena, D.E. Resasco, *J. Catal.* 277 (2011) 1–13.
- [52] J. Greeley, T.F. Jaramillo, J. Bonde, I. Chorkendorff, J.K. Nørskov, *Nat. Mater.* 5 (2006) 909–913.
- [53] P. Liu, J.A. Rodríguez, *J. Am. Chem. Soc.* 127 (2005) 14871–14878.
- [54] T.-T. Zhuang, Z.-Q. Liang, A. Seifitokaldani, Y. Li, P. De Luna, T. Burdyny, F. Che, F. Meng, Y. Min, R. Quintero-Bermudez, C.T. Dinh, Y. Pang, M. Zhong, B. Zhang, J. Li, P.-N. Chen, X.-L. Zheng, H. Liang, W.-N. Ge, B.-J. Ye, D. Sinton, S.-H. Yu, E.H. Sargent, *Nature Catal.* 1 (2018) 421–428.
- [55] X. Qizhong, W. Yun, L. Peng-Fei, Z. Li-Rong, W. Guozhong, Y. Hua-Gui, W. Po-Keung, Z. Haimin, Z. Huijun, *Adv. Mater.* <https://doi.org/doi.org/10.1002/adma.201801450>.
- [56] J.-H. Kim, D.H. Youn, K. Kawashima, J. Lin, H. Lim, C.B. Mullins, *Appl. Catal. B. Environ.* 225 (2018) 1–7.
- [57] M. Yao, N. Wang, W. Hu, S. Komarneni, *Appl. Catal. B. Environ.* 233 (2018) 226–233.
- [58] F. Hu, S. Zhu, S. Chen, Y. Li, L. Ma, T. Wu, Y. Zhang, C. Wang, C. Liu, X. Yang, L. Song, X. Yang, Y. Xiong, *Adv. Mater.* 29 (2017) 1606570–1606579.
- [59] B. You, X. Liu, N. Jiang, Y. Sun, *J. Am. Chem. Soc.* 138 (2016) 13639–13646.